C. R. Physique 13 (2012) 316–327

Contents lists available at SciVerse ScienceDirect

Comptes Rendus Physique

www.sciencedirect.com

Use of large scale facilities for research in metallurgy

Three-dimensional characterisation and modelling of small fatigue corner cracks in high strength Al-alloys

Caractérisation et modélisation 3D des fissures courtes de fatigue de coin dans des alliages d'aluminium à haute résistance

Henry Proudhon [a], A. Moffat [b], Ian Sinclair [b], Jean-Yves Buffiere [c,*]

[a] *MINES ParisTech, centre des matériaux, CNRS UMR 7633, BP 87 91003 Evry cedex, France*
[b] *School of Engineering Sciences, University of Southampton, UK*
[c] *Université de Lyon – INSA Lyon, MATEIS, 20, avenue A. Einstein, 69621 Villeurbanne cedex, France*

ARTICLE INFO

Article history:
Available online 27 January 2012

Keywords:
Fatigue
Computed tomography
Synchrotron radiation
Crack closure
Aluminium alloys

Mots-clés :
Fatigue
Tomographie
Rayonnement synchrotron
Fermeture des fissures
Alliages d'aluminium

ABSTRACT

The growth of fatigue cracks at small length scales is known to be influenced by a variety of factors, including local microstructure, varying stress states and crack shape. High resolution computed tomography allows for sub-micron resolution imaging of failure processes in small test coupons undergoing in situ cyclic loading, providing detailed three-dimensional (3D) assessment of propagation processes across the entire crack front (surface and depth). In this work fatigue crack growth has been examined in an advanced Direct Chill (DC) cast aluminium alloy, along with a fine grained powder-metallurgy alloy. The latter is identified as a model material, offering considerably simpler microscopic crack paths than the DC cast alloy, and hence a means of separating bulk mechanical effects (such as stress state variations across a crack front and plasticity induced closure) from microstructural effects (such as crystallographic deflection and roughness induced crack closure). Crack growth has been studied in both materials under both constant amplitude (CA) and single peak overload (OL) conditions. Experimental results are presented in the present paper, particularly in relation to micromechanical understanding of failure. A modelling approach based on those results, and some typical results, is also presented.

RÉSUMÉ

La croissance des fissures courtes de fatigue est fortement influencée par un grand nombre de facteurs tels que la microstructure environnante, l'état de contrainte local, la forme des fissures. La tomographie haute résolution permet d'imager la propagation des fissures dans des éprouvettes de fatigue au cours d'essais in situ avec une résolution spatiale sub micronique et permet ainsi de visualiser les processus de propagation le long de la totalité du front de fissure (en surface *et* en volume). Dans ce travail, la croissance des fissures de fatigue a été caractérisée dans un alliage d'aluminium à haute résistance élaboré par coulée continue ainsi que dans un alliage à grain fins élaboré par métallurgie des poudres. Ce dernier matériau constitue un matériau modèle qui présente des formes de fissures considérablement plus simples que dans l'alliage à gros grains ce qui permet de séparer les effets purement mécaniques (variation de l'état de contrainte le long du front et fermeture induite par la plasticité) des effets purement microstructuraux (tels que les déflexions

* Corresponding author.
E-mail addresses: henry.proudhon@mines-paristech.fr (H. Proudhon), I.Sinclair@soton.ac.uk (I. Sinclair), jean-yves.buffiere@insa-lyon.fr (J.-Y. Buffiere).

1631-0705/$ – see front matter
doi:10.1016/j.crhy.2011.12.005

locales et la fermeture par rugosité). Pour les deux alliages, la croissance des fissures a été étudiée lors d'essais cycliques à amplitude de contrainte constante, ponctués par des essais de surcharge (sur un cycle unique). Nous présentons ici un résumé des principaux résultats obtenus du point de vue expérimental. Une modélisation de la propagation 3D des fissures est également décrite ainsi que certains des résultats que cette approche simplifiée a permis d'obtenir.

1. Introduction

The growth of small fatigue cracks (sub-millimetre) is recognised as critical in many engineering situations [1,2]. When damage arises from the corner of a stress concentrating feature, such as fastener locations found in metallic airframes, failure is conventionally identified with simple quarter-circle or quarter ellipse defect shapes [3], subsequently evolving into through-thickness cracks. There is a general understanding that in comparison to large defects, crack growth at such small scales is influenced by several factors; these include microstructural features (e.g. grain size and shape, boundary misorientation and second phase particle distribution) and (micro-)mechanical aspects (e.g. stress intensity variations across non-linear crack fronts, stress state, crack closure) [4].

Current capabilities in synchrotron radiation computed tomography (SRCT) imaging [5] have been shown to provide highly informative three-dimensional (3D) quantification of fracture process in various structural materials [6–10]. This simultaneously obviates the experimental uncertainty in conventional surface-based and/or post-mortem crack growth studies, whilst providing novel opportunities for the precise local mapping of crack morphologies and behaviour with respect to microstructural and micromechanical environment.

The current work seeks to apply SRCT imaging to the growth of small corner fatigue cracks, focusing on a post-initiation regime, with crack lengths of the order of 100–1000 μm. Both constant amplitude and single peak overloads are used to interrogate growth behaviour. To assist in the separation of microstructural and continuum mechanics contributions to crack growth, tests are carried out on both an advanced commercial airframe alloy (AA2027) produced by the conventional DC casting route, and a "model" fine grained material (AA5091) produced by mechanical alloying and known to exhibit relatively ideal flat crack profiles [11]. Crack growth under both constant amplitude and single peak overloads was examined. These observations are considered in terms of local micromechanical behaviour and a framework for closure-based crack growth modelling previously reported by the authors for long crack growth in conventional airframe aluminium alloys [12–17]. To maintain engineering relevance, the modelling framework adopts a multi-mechanistic, but computationally simple approach to the combined action of roughness and plasticity induced crack closure.

2. Experimental methods

2.1. Materials

AA2027 is a high purity (low Fe and Si content) variant of the widely used AA2024 alloy, see Table 1. The material was tested in the T351 condition, in 40 mm gauge plate, with a low recrystallised fraction (8%) characteristic of commercial product. The anisotropic grain dimensions have been measured optically at the mid-thickness position as 592 μm, 223 μm and 40 μm in the L, T and S directions respectively (mean linear intercepts). Electron backscatter diffraction (EBSD) revealed a characteristic strong rolling texture.

The nominal composition of AA5091 is shown in Table 1. This alloy has a limited age hardening capacity, largely deriving its strength from a refined, mechanically alloyed microstructure and a high volume fraction of non-shearable oxide and carbide dispersoids [11]. It exhibits a predominantly micron to sub-micron grain size, although larger grains (between 2 and 50 μm) are present, making up some 25% of the material bulk. Yield strengths of the two materials are not identical, but are of a similar order: 430 and 370 MPa for AA5091 and AA2027 respectively. The ultrafine grains promote homogeneous deformation and prevent crystallographic cracking so that the crack shape is not disturbed by microstructural features, at least not at the level of the spatial resolution employed in this study [11].

2.2. Experimental procedure

High resolution synchrotron X-ray tomography was carried out at beamline ID19 of the European Synchrotron Radiation Facility (ESRF) to obtain three-dimensional images of small corner fatigue cracks. The elements of the tomography

Table 1
Chemical composition (wt%) of the two alloys used.

Material	Cu	Mg	Mn	Zr	Fe	Si	Li	O	C
AA2027	4.3	1.3	0.65	0.1	0.09	0.05	–	–	–
AA5091	–	4.0	–	–	–	–	1.3	0.8	1.1

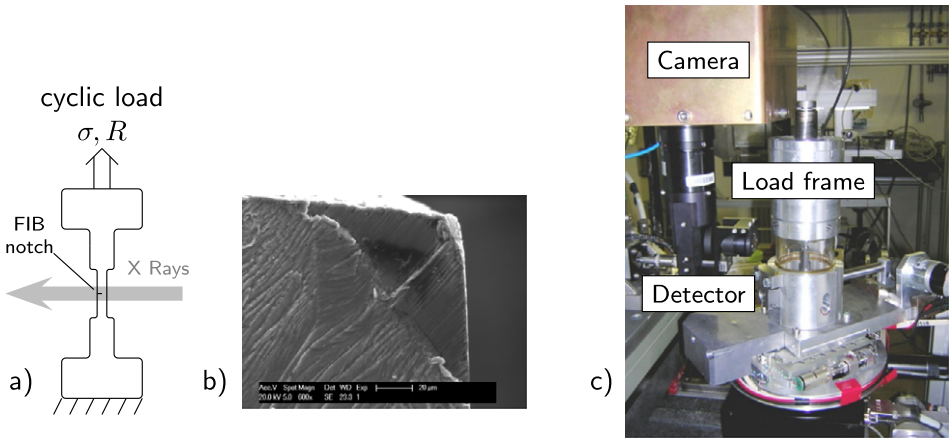

Fig. 1. Key elements of the tomography setup: a) specimen schematics showing the imaged region of interest around the FIB notch; b) detail of the FIB notch as seen on an SEM micrograph of a failed sample; c) photograph of the loading device and detector arrangement (sample is visible through Perspex tube section).

experimental set up of ID19 can be found in Ref. [18]. In the following paragraphs, only the main experimental features are presented. Obtaining a tomographic image consists, firstly, of recording a series of radiographs (called a scan) of a sample which is rotated around one axis. These radiographs are further used by a reconstruction algorithm to obtain a 3D numerical image of the sample which is, in its classical form, a 3D map of the attenuation coefficient in the sample. The two-dimensional (2D) radiographs are recorded on a Charge Coupled Device (CCD) camera with a square array of 2048×2048 elements. This detector is coupled with a fluorescent screen via optical lenses. The white beam coming from the synchrotron ring is rendered monochromatic by a multilayer monochromator. The monochromatic beam is parallel so no geometric enlargement is possible, instead, the voxel size is a result of the camera optics used. A detailed presentation of the technique and some typical applications in materials science can be found in [19].

A dedicated fatigue machine with a reduced size and a low vibration level has been designed in order to monitor crack development in situ. The machine uses an X-ray transparent load frame [20] positioned in the beamline, running at a frequency of 50 Hz. It was directly installed on the rotation stage of the micro-tomography setup (see Fig. 1c).

Small tension–tension samples were utilised,[1] as illustrated in Fig. 1a, oriented in the primary working direction of both materials. Most of the samples were of a 1×1 mm^2 cross-section, providing an isotropic voxel size of 0.7 µm when using a 2048×2048 resolution FReLON detector [21]. A sample to detector propagation distance of 15 cm was used with an incident beam energy of 20.5 keV; as such phase enhanced images were obtained in the so-called edge-detection regime (near-field Fresnel diffraction). All cracks were initiated from very sharp focused ion beam (FIB) corner notches; notch widths were of the order of a few micrometers, at depths of the order of 20–50 µm (see Fig. 1b). Sample surfaces were polished to a 1 µm finish to ensure initiation was dominated by the FIB defects in the region of interest. Once crack growth had been seen to occur from the FIB defects, crack length was monitored using simple radiographic projection between Computed Tomography (CT) scans.

Tests were carried out at ΔK baseline levels between 2 and 3 MPa$\sqrt{\text{m}}$. Between the individual samples (seven in total), the following experimental goals were addressed:

(i) characterise R-ratio effects on constant amplitude crack growth at low (0.1) and high (between 0.5–0.7) cyclic stresses values;
(ii) perform single overloads (100%, as defined by maximum overload and baseline loads) and investigate the effect on subsequent propagation;
(iii) collect local 3D information (local surface contact points/areas, crack orientation, local acceleration or deceleration) to gain insight into crack propagation mechanisms.

CT scans were performed periodically with the specimen being held temporarily at maximum load (scan times were around 30 minutes). Holding the samples at maximum load during the scan was used to improve accuracy in length/shape measurement (maximum opening of the crack).

2.3. 3D data processing

The X-ray tomography technique generates large amounts of data that, unlike classical 2D images, requires significant post-treatment. The images however offer various opportunities for novel quantitative analysis, such as 3D "full field" map-

[1] The load ratio R is defined as the ratio between the minimum (σ_{min}) and the maximum (σ_{max}) loads applied during the fatigue test. A tension–tension test corresponds to a positive value for σ_{min} i.e. $R > 0$.

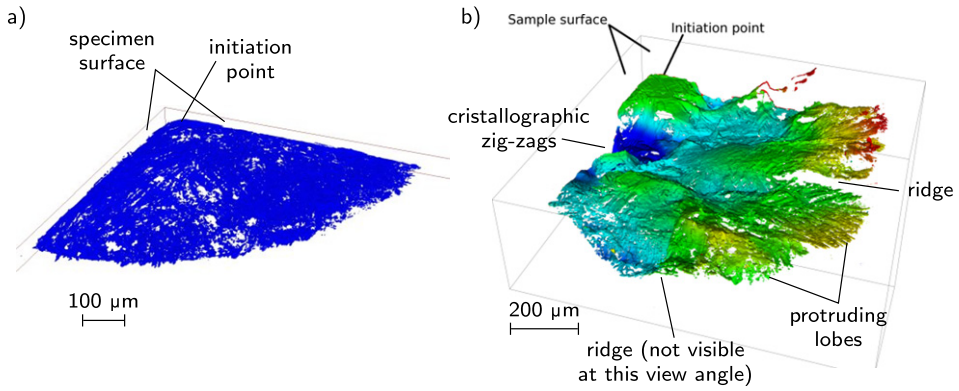

Fig. 2. Three-dimensional rendering of fatigue cracks imaged by SRCT in both alloys (the colour indicates the height of the crack in the sample): a) crack in the 5091 alloy, the crack length is 500 µm, the crack surface is highly planar; b) crack in the 2027 alloy, the crack length is 700 µm, a more irregular crack surface is observed.

ping of crack opening against local growth rates and directions. Such quantitative analysis, coupled to the large amount of data gathered in the current experimental programme (around one hundred high resolution CT scans corresponding to approximately 1 Terabyte of data) brings the need to design specific image analysis routines to compute and extract key parameters, as well as automatically produce crack images. In analysing CT volumes *region growth* algorithms [22] are often employed to obtain a binary image of the crack (a process called segmentation); such algorithms merge the neighbouring voxels contained in the crack and require, therefore, that all the crack branches are connected [11]. This usually holds true if the crack is very open. For the AA2027 material, levels of apparent crack closure were high enough to prevent the use of region growing algorithms, especially near the crack tip, the determination of which is of primary importance within this project (see below). Instead classical grey level thresholding was used, iteratively combined with crack height filtering. This proved to significantly improve the crack shape determination v.s. region growing algorithm. Segmented volumes were then processed using inhouse VTK[2] routines to obtain 3D renderings of the cracks.

Crack tip location: Distinguishing the tip of a small, low stress intensity fatigue crack is always problematic. Surface analyses potentially suffer from polishing artefacts and/or crack closure at the tip. Whilst with tomographic data polishing is not an issue, the resolution is significant. 0.7 µm voxel imaging at ID19 has been shown to be quite accurate in capturing small/fine cracks in metallic samples [18]. This is partly due to phase contrast generated at the crack surfaces, which appears on the reconstructed images as a narrow band of white contrast, as opposed to the black contrast band within the crack [23]. Thus, crack regions experiencing sub-voxel opening level (typically close to the crack tip) will produce only the white phase contrast allowing the eye to still pick up the tip location reasonably well; in practice however, this is difficult to distinguish via automated/thresholding methods. Extracting the crack front in the present data has therefore required manual intervention, which was done in the AA2027 by browsing the volumes every 5 slices and picking up the crack tip location by eye. In spite of the amount of manual work required, this method was evaluated as the best (at present at least) to robustly assess the crack tip position in such a material. In the AA5091 samples the process was more straightforward given the relatively flat crack shapes, however manual intervention was again involved. Repeated measurements and manual estimation of the maximum and minimum rational crack front locations in numerous images indicated that local crack lengths could be determined to an accuracy of the order of 3 µm in the AA5091, whilst an error of the order of 7 µm was identified for the more complex AA2027 cracks. Two sets of successive crack front positions are shown in Fig. 3 for the two investigated alloys; they correspond to projections of the crack area on the plane normal to the loading direction.

3. Results and analysis

Typical fracture morphologies of the AA5091 and AA2027 materials are shown in Fig. 2. Significant differences are evident, with AA2027 showing deflections and bifurcations over length scales up to ∼200 µm, previously identified with crystallographic failure across the relatively coarse grain structure of this material [14]. The AA5091 crack is highly planar by comparison; SEM observation reveals a much finer degree of surface roughness, with features of the order of 1–10 µm.

3.1. Crack propagation

3.1.1. Constant amplitude growth

AA5091 behaviour: Fig. 3a provides a detailed record of crack evolution in AA5091 at a baseline R-ratio of 0.1. In terms of overall crack shape, it was seen that the AA50591 cracks had very simple shapes. Prior to the overload and when the crack

[2] The visualisation toolkit http://vtk.org.

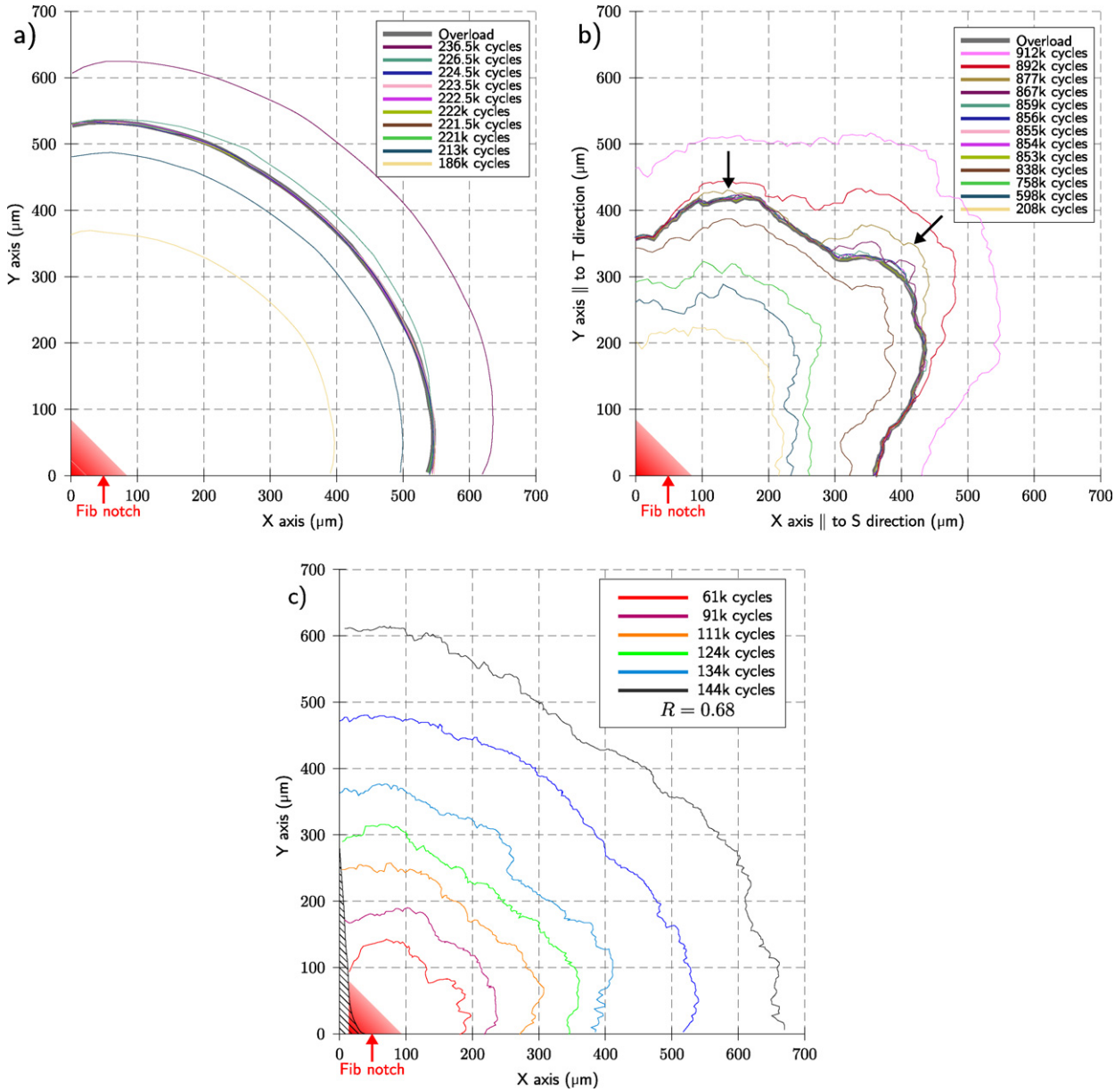

Fig. 3. Representative crack front evolution observed in (a) AA5091, and (b, c) AA2027, highlighting the more complex crack shape of the coarse grained material, the post-overload retardation that occurs in both materials, and the degree of surface pinning/retardation at the free surfaces in both alloys. Arrows in (b) indicate locations of preferential post-overload growth in AA2027. The hatched area in (c) indicates a loss of material (compared to a perfect square section) caused by mechanical polishing. The T and S direction refer to the Transverse and Short directions in the sheet from which the samples were cut.

size a is lower than half of the sample width W ($a/W < 0.5$), over 90% of the crack front falls within ∼1% of an ideal quarter-circular profile in Fig. 3a. Towards the specimen surfaces there is a slight pinning/retardation extending some 40 and 60 µm from the free surface, with surface crack lengths being identified as ∼2–3% shorter than those in the specimen bulk.

AA2027 behaviour: Crack fronts in AA2027 are compared in Figs. 3b and 3c for low and high R-ratios (0.1 and 0.68 respectively). From Fig. 3b it is particularly evident that even at a maximum crack length of 700 µm (45° position within the specimen bulk), crack fronts at $R = 0.1$ are distinctly irregular, departing significantly from a quarter-circular or quarter elliptical form. Strong pinning is evident towards the specimen surfaces, along with pronounced local "bulges" of crack extension being seen within the specimen bulk (arrows in Fig. 3b). At comparable lengths (∼200–500 µm), growth at the high R-ratio of 0.68 is illustrated in Fig. 3c, establishing a more regular shape, and less pronounced pinning is evident at the specimen surfaces compared with the 0.1 data.

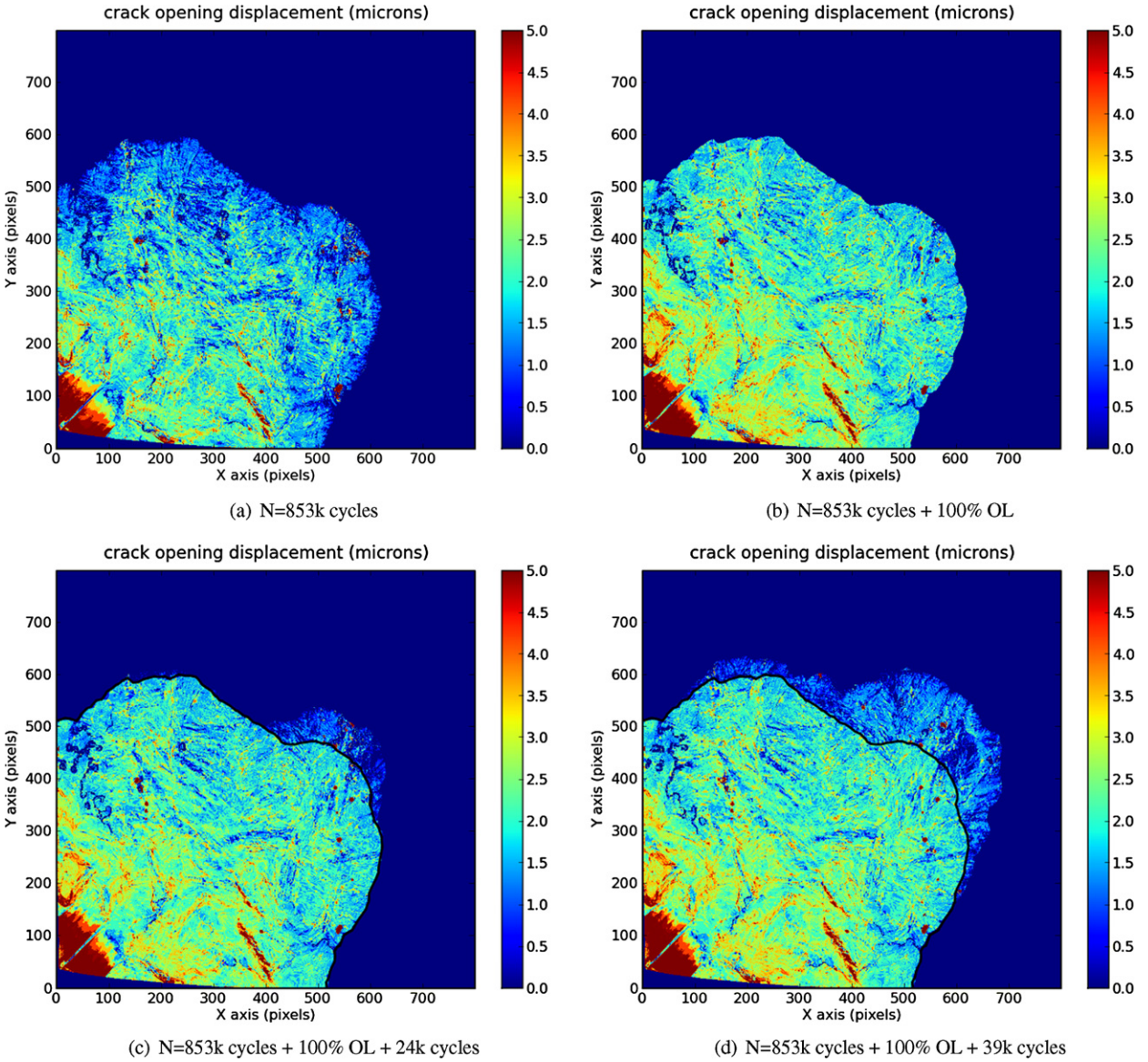

Fig. 4. Maps of the crack opening displacement at various crack propagation stages: a) before OL, b) immediately following OL, c) 24k cycles after OL, d) 39k cycles after OL.

3.1.2. Post overload behaviour

AA5091 behaviour: Fig. 3a shows the effect of a single 100% overload (OL) cycle applied to the AA5091 material (applied at 221k cycles), located by the thick grey line. It can be seen that crack growth arrest occurred for some 3.5k cycles across the whole crack front: after a further 2k cycles growth is seen to restart across the central part of the crack front, but arrest is still evident at the sample surfaces. After some 5.5k cycles, growth is seen across the whole crack front, although a degree of retardation is evident at the specimen surfaces (surface length ∼5% less than in the bulk, as opposed to 2–3% under constant amplitude growth).

AA2027 behaviour: The position of the crack front at overload in Fig. 3b is again highlighted with a thick grey line. From the subsequent crack fronts, it is clear that the crack experiences enhanced retardation close to the surface, similar to, but more pronounced than in AA5091. It is also evident that the crack again stops for a few thousand cycles on application of the overload. Crack growth then resumes, but only at two places within the bulk highlighted by arrows on Fig. 3b. The growth in those regions remains local for a few tens of thousand of cycles after which they merge (after 39k cycles). At this point the crack is still pinned at the surface. After some 59k cycles crack growth has resumed in the whole specimen.

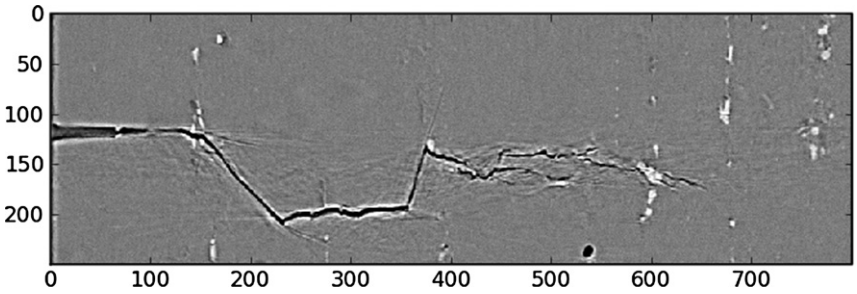

Fig. 5. Crack deflection in 2027 alloy.

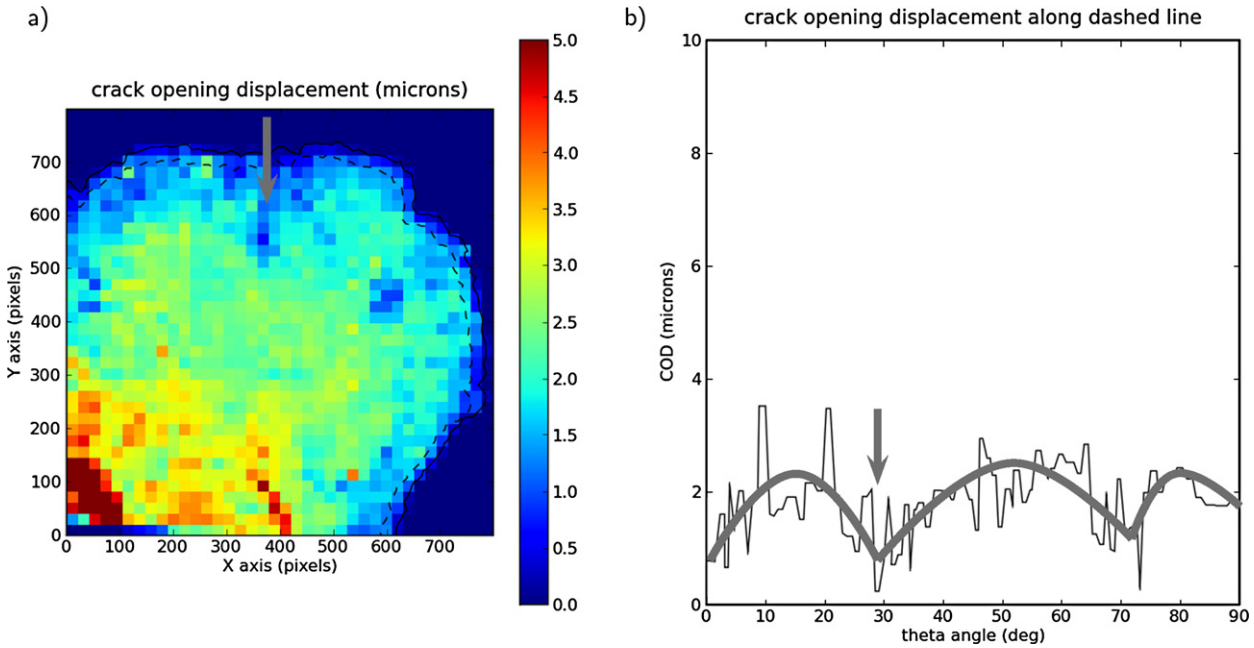

Fig. 6. Example of local crack opening displacement measurement in AA2027: a) COD map of the crack in the final stage (912k); b) plot of the crack opening 20 micrometers behind the crack tip (see dashed line on the left image).

3.1.3. Crack path, opening and growth behaviour in AA2027

Fig. 4 shows maps of the crack opening prior to and after the 100% overload in AA2027 alloy. In the fine grain material opening mapping was considered relatively inaccurate, due to the very small openings and strong phase contrast effects produced by the planar crack shape. Slower crack growth was frequently observed in the AA2027 in the zones of the crack front where opening was smaller (Fig. 6). After the overload, the opening of the crack considerably increased (Fig. 4c) and appeared almost constant (∼1.5–2 μm) along the crack front, at least with the spatial resolution used (∼ twice the voxel size i.e. around 1.4 μm).

As mentioned previously, the crack path in AA2027 was very tortuous with strong deviations (see Fig. 5) probably associated with the presence of grain boundaries. At the crack front, such deviations created independent branches between which ridges (with a typical length of ∼50–100 μm) were created (Fig. 2). Near such ridges a smaller crack opening was usually measured (see Fig. 6). After the overload, the zones where crack growth first occurred post-overload, were already regions of accelerated constant amplitude growth (bulges along the crack front), particularly where height mapping shows these to be relatively flat regions oriented at 90° with respect to the applied stress (mode I opening).

3.1.4. Analysis

AA5091 behaviour: As a model material, exhibiting limited local microstructural influence on crack path, the incidence of a uniform and simple crack shape may be seen as underlying support for the use of simple crack shape stress intensity calculations. The apparent stability of this crack shape is, however, not consistent with the associated stress intensity solutions (e.g. see [24]). Stress intensities for an ideal quarter-circle crack increase from the centre/45° position towards the specimen

surfaces.[3] For intermediate crack length conditions ($a/W \sim 0.5$) stress intensities are some 15% higher near the sample surfaces: for typical Paris law exponents (between 2 and 4), instantaneous surface crack growth rates should be between 30% and 75% faster towards the surfaces, i.e. a quarter-circle crack should not grow in a stable/self-similar manner. Crack shape evolution arising from such stress intensity profiles can be identified with an initial dynamic interaction between growth and crack shape, eventually giving rise to a stable shape that, in the absence of crack closure, is a function of elastic fracture mechanics (particularly Poisson's ratio and sample thickness).

The widely observed retardation of fatigue cracks close to free surfaces in thick samples [25] is identifiable with changes in stress state [24,26–30], commonly related to increased plasticity induced crack closure (PICC) levels associated with (near) plane stress deformation at/near a free surface. Given the dependence of calculated stress intensities on position within a sample, and the stress state influence on closure levels, the appearance of a stable circular shape may then be identified with a balance between these effects. With the present simple AA5091 crack shapes it is possible to make accurate use of a quarter-circle K solution for the central portion of the crack, away from the surface pinning [31]. Examining local crack growth rates at the centre/45° position as a function of applied R-ratio shows growth for $R = 0.5, 0.57$ and 0.66 in the AA5091 is accelerated in relation to $R = 0.1$ data, but fall together closely (within experimental scatter). This is readily interpreted as the three high R-ratios being closure free at this location in the sample (K_{min} exceeding K_{cl}).[4] Equating equal ΔK_{eff} conditions with equal $\mathrm{d}a/\mathrm{d}N$ values at different R-ratios, a closure condition of $K_{cl}/K_{max} \sim 0.38$ is then derived for the centre/45° position at $R = 0.1$. Surface stress intensities may be known with less certainty, for example Branco et al. [30] show the sensitivity of near surface K values to pinning. However, estimates for PICC closure under plane stress conditions are well established. For an R-ratio of 0.1 the classical modelling of Budianski and Hutchinson indicates a condition of $K_{cl}/K_{max} \sim 0.48$ [33]. Given the K_{cl}/K_{max} value of 0.38 estimated for the sample centre, this implies a drop of ∼16% in ΔK_{eff} between surface and centre locations for a given applied ΔK. As such, crack closure effects may indeed closely compensate for the near-surface rise in stress intensities for a quarter-circular crack profile, consistent with the stability of crack shape in Fig. 3a.

Given the very flat AA5091 crack morphology, a centre/45° position K_{cl}/K_{max} value of 0.38 bears some justification, as: (a) plasticity induced crack closure (PICC) effects would be expected to be minimal for the associated plane strain conditions [12,24], and (b) limited fracture surface deflection would be expected to limit roughness induced crack closure (RICC) effects [34]. The low stress intensities of the current work should be noted however, with results by Venkateswara and Ritchie [35] for example, yielding very similar closure levels for the same stress intensity levels in large, plane strain dominated samples of similar mechanically alloyed material. The finite element and analytical modelling results of Kamp et al. [13] further show that for RICC to operate effectively, surface feature sizes should approach the maximum plastic zone size for the load conditions in question. In this case the plane strain plastic zone size is the order of 5 μm, with the AA5091 fracture surface showing features of this order or larger.

AA2027 behaviour: Distinctive features of the AA2027 crack shapes at low R-ratio may be summarised as strong pinning at the free surfaces, and local irregular protuberances (or bulges) occurring within the specimen bulk. Conversely, both these effects are significantly ameliorated at high R-ratio, with crack shapes approaching that of the AA5091 tests. In the first instance, these changes appear consistent with: (a) increased local microstructure influence as crack length scales approach those of the underlying microstructure, and (b) changes in the balance between surface and bulk ΔK_{eff} levels, particularly for the $R = 0.1$ condition.

Whilst local crystallography, deflection shielding and bifurcation can all be expected to contribute to local crack growth processes in the AA2027, the influence of R-ratio implies that local RICC effects are a significant source of crack front irregularity, i.e. irregularity was most pronounced at low R-ratio, occurring on a scale comparable to the major surface deflections. This is supported by local crack opening measurements, as illustrated in Fig. 6, where it was frequently (but not exclusively) observed that areas of slower crack growth rate corresponded to ridges along the crack wake exhibiting reduced crack opening (see arrow in Fig. 6).

As mentioned above, the strong crack deflection observed in the AA2027 alloy are probably linked to the crossing of grain boundaries. However, in its classical form, tomography is not sensitive to crystallographic orientations and cannot in principle reveal the 3D texture of materials as EBSD can do, for example, on a polished surface. This problem can be partly circumvented, in Al alloys, using a technique which decorates grain boundaries with gallium. The 3D shape of the grains which can be obtained by this method can be used to assess the effect of grain boundaries on the initiation and propagation of small fatigue cracks [14,18,36]. By using the Ga infiltration technique, it is possible to correlate protruding or retarded parts of 3D crack fronts with the presence of grain boundaries. The ability of a microstructurally small crack to propagate faster/slower in some grains is linked to the ease/difficulty of activating small scale plasticity in the adjacent grains as suggested, for instance, by Newman [2]. The knowledge of the local crystallographic orientation is necessary to check this assumption. This orientation can now be obtained by Diffraction Contrast Tomography (DCT), a non-destructive characterisation technique that is a variant of tomography also developed at ESRF [37] (on this technique, see also the

[3] For the purposes of this paper, the exact singularity for a crack emerging at a given angle at a free surface will not be considered: for simplicity/brevity, stress intensities close to free surfaces will be taken as a reasonable estimate of local crack driving force.

[4] Crack closure corresponds to the crack being closed under non-zero load. Various physical mechanisms can account for this phenomenon [32]. Crack closure induces a reduction of the crack driving force (the stress intensity factor range ΔK) from $\Delta K_{nom} = K_{max} - K_{min}$ to an effective value $\Delta K_{eff} = K_{max} - K_{op}$. The K value corresponding to the opening/closing of the crack is called K_{cl} [32].

paper by Ludwig et al. in the same volume). First results have been obtained on a Ti alloy. Images of a short fatigue crack propagating in a fully characterised subset of grains (3D shape and orientation) have been obtained. They show that the propagation of a small crack is a highly 3D process and that, because of the continuity of the crack front, the growth of a crack in a given grain is strongly influenced by the difficulty/ease of growing in the neighbouring grains [38]. Modelling small crack growth from this data remains challenging as the first results tend to indicate that a macroscopic approach based on a Schmid factor calculated in each grain of the crack front, for example, does not allow to predict the activated slip planes (crack facets), probably because of the complex local stress state induced at the crack front [38]. Crystal plasticity simulations based on the real microstructure of the sample might help to solve this problem [39], but it is still a challenging approach in terms of computation time and complexity. In the following section a more simple and macroscopic modelling approach is presented.

4. Crack growth modelling

As noted earlier, a simplified analytical framework for closure-based modelling of long crack growth has been reported previously by the authors [12–17]. A full review is beyond the scope of this paper, and the reader is referred to the earlier works. In brief summary, it has been shown via elastic–plastic finite element analysis that, in deflected (zig-zag) cracks, residual plastic shear displacements may remain at asperity tips in the crack wake. The residual shear displacements can be said to form a wedge at the tip of asperities and the size/height of these wedges is closely related to the crack tip shear displacement (CTSD). In the proposed analytical representation the assumption is made that when the wedge height is equal to the local crack opening displacement (COD), upper and lower surfaces of the crack wake are in contact and RICC occurs. Singh et al. [15] further identified that PICC due to OLs was related to the above RICC description, in that, on the application of an overload, a wedge of material may be considered to be left in the crack wake. In the PICC OL case the height of the wedge is directly related to the crack tip opening displacement (CTOD) at the point of overload.

In considering CTOD and CTSD values to represent first order estimates of residual crack flank deformation associated with PICC and RICC processes under constant amplitude and overload crack growth, a simple analytical multi-mechanistic description of closure behaviour was established. As the associated analytical models are produced using established linear elastic fracture mechanics equations it was relatively simple to repeat their derivations for plane stress and plane strain equations, with the micromechanics of the models remaining the same. This led to expressions for RICC under constant amplitude (CA) and OL conditions and under plane stress and plane strain conditions, along with PICC expressions for OLs under plane stress and plane strain conditions. For a full description of crack growth in small plane sided samples such as those tested here, PICC conditions for CA growth are also required. Established results for CA PICC under plane stress were noted in Section 3.1 above, with the strip yield results of Budiansky and Hutchinson [33] being utilised here. For CA PICC under plane strain, we note zero/negligible closure levels based on previous FE results [12,17]. As a final step, we must identify how the individual model components (i.e. addressing PICC/RICC in plane stress/plane strain for CA and OL growth) may act together. Based on earlier work [15], we identify a simple competition between closure mechanisms, where it is simply the strongest closure processes acting at a given point in the load history that controls growth behaviour.

The models contain various potential fitting parameters [12,13,15,17]. These may be related to: (a) crack-tip deformation mechanics for each closure mechanism (PICC and RICC) and stress state, and (b) materials parameters, representing crack tortuosity. The former parameter group may be shown to be obtainable from conventional long crack tests of the AA2027 material, independent of the current small sample tests. In terms of crack tortuosity, previous works [16] have considered fracture surface deflections in terms of two characteristic angles, θ and ψ (corresponding to deflection in the direction of growth and twist perpendicular to the growth direction) and a characteristic length, L, and sought to estimate them from direct surface measurements. In the interest of simplicity, in the present work, only deflection in the direction of growth θ, and the length L, were considered.

An important specification of the modelling was that, whilst the experimental part of the project dealt with detailed 3D quantification of crack shape, the modelling sought to avoid correspondingly detailed stress intensity calculations. Aiming at a simpler approach amenable to engineering application, a simple crack shape was employed to assess the stress intensity factors. Crack propagation was then modelled as follows:

(i) A quarter-circle crack shape was assumed and stress intensities calculated along the front, discretised into 1° angular elements;
(ii) PICC and RICC calculations were made for both plane stress and plane strain conditions, with plane stress being associated with the surface crack locations. CA closure conditions were considered, along with any prior load transients;
(iii) Linear interpolation was used to transition between the surface (plane stress) and sub-surface (plane strain) closure levels, occurring over an assumed distance of two surface plastic zone radii;
(iv) The crack extension $\mathrm{d}a/\mathrm{d}N$ was calculated around the crack front based on ΔK_{eff}, drawing on previously established $\mathrm{d}a/\mathrm{d}N$ vs. ΔK_{eff} data;
(v) Overall crack length was updated based on equivalent areas: a new quarter-circle crack is generated and used for the next crack growth calculation.

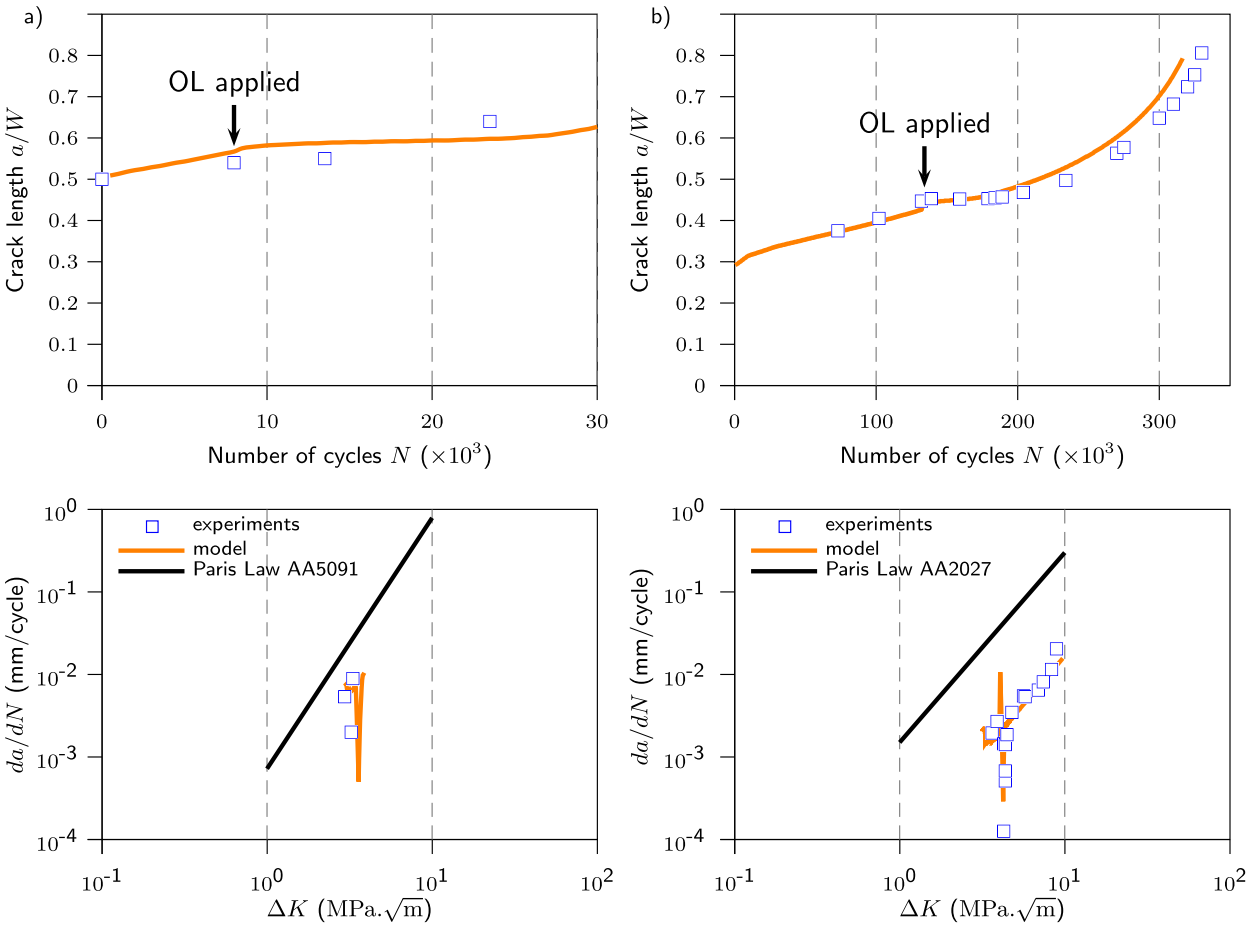

Fig. 7. Comparison of crack growth predictions, obtained by the model at $R = 0.1$ with a single OL, vs. experimental results based on equivalent area measurements a) AA5091, b) AA2027.

Representative comparisons of experimental and modelled da/dN for the AA5091 and AA2027 material are shown in Fig. 7. In particular, it is seen that CA and post OL behaviour is reasonably well approximated. In terms of the more demanding representation of OL behaviour, the exact fit between model and experimental data was seen to vary with individual tests. Importantly, it was found that by representing the two very different alloys tested here by only two micromechanical parameters for each (θ and L), OL transients were consistently predicted within a single mechanistic framework (and corresponding single set of fitting parameters) to within ∼50% in terms of number of delay cycles (cycles to re-establish baseline growth). As such the generalisation capability implied by the mechanistic basis of the model appears to be born out, bearing in mind the distinct simplifications adopted in implementation (such as the simple linear transition of stress states between surface and bulk and the equivalent area crack length description).

5. Conclusion

A detailed experimental and modelling study regarding small corner crack growth under fatigue loading has been presented. High resolution X-ray tomography was used extensively to retrieve the 3D crack shape throughout the fatigue lives of the samples. Two materials with markedly different microstructures were used to differentiate between microstructurally based mechanisms and continuum mechanics effect, such as surface/bulk stress states. In AA5091, it was found that cracks developed with a largely ideal, flat shape that agreed well with basic crack mechanics and closure understanding. In the 2027 alloy, crack fronts were seen to be highly irregular at length scales up to several hundred micrometres, with distinctive local pinning occurring at both free surfaces and at internal areas of rougher crack growth. In particular, the influence of local roughness induced closure has intimated via R-ratio influence and CT assessment of crack shape and opening behaviour.

It was the aim of the present work to extend previous multi-mechanistic closure modelling of large, through-thickness cracks to the growth of small corner defects (from 100 μm to 1 mm in size). Overall, it has been possible to simulate baseline crack growth in each experimental case well, with overload delay transients being predicted to within a factor of

two (in terms of number of cycles); this is considered to be within reasonable expected error when accounting for various simplifications adopted to maintain engineering applicability.

Acknowledgements

The authors would like to thank Airbus UK for funding this project and D. Dai and R. Collins for useful conversation. The authors also acknowledge G. Johnson and E. Boller from beamline ID19 at ESRF for their help with experiments.

References

[1] S. Suresh, R.O. Ritchie, Propagation of short fatigue cracks, International Metals Reviews 29 (6) (1984) 445–476.
[2] J.C. Newman Jr., The merging of fatigue and fracture mechanics concepts: a historical perspective, Progress in Aerospace Sciences 34 (5–6) (1998) 347–390.
[3] L.G. Zhao, J. Tong, J. Byrne, Stress intensity factor K and the elastic T-stress for corner cracks, International Journal of Fracture 109 (2) (2001) 209–225.
[4] D. Davidson, K. Chan, R. Mc Clung, S. Hudak, Small fatigue cracks, in: I. Milne, R.O. Ritchie, B. Karihaloo (Eds.), Comprehensive Structural Integrity, Pergamon, Oxford, 2003, pp. 129–164.
[5] S. Stock, MicroComputed Tomography: Methodology and Applications, CRC, 2008.
[6] A. Guvenilir, T.M. Breunig, J.H. Kinney, S.R. Stock, Direct observation of crack opening as a function of applied load in the interior of a notched tensile sample of Al–Li 2090, Acta Materialia 45 (5) (1997) 1977–1987.
[7] H. Toda, I. Sinclair, J.-Y. Buffiere, E. Maire, K.H. Khor, P. Gregson, T. Kobayashi, A 3D measurement procedure for internal local crack driving forces via synchrotron X-ray microtomography, Acta Materialia 52 (5) (2004) 1305–1317.
[8] R. Sinclair, M. Preuss, E. Maire, J.-Y. Buffiere, P. Bowen, P.J. Withers, The effect of fibre fractures in the bridging zone of fatigue cracked Ti–6Al–4V/SiC fibre composites, Acta Materialia 52 (6) (2004) 1423–1438.
[9] H. Zhang, H. Toda, H. Hara, M. Kobayashi, T. Kobayashi, D. Sugiyama, N. Kuroda, K. Uesugi, Three-dimensional visualization of the interaction between fatigue crack and micropores in an aluminum alloy using synchrotron X-ray microtomography, Metallurgical and Materials Transactions A 38 (8) (2007) 1774–1785.
[10] Y.-C. Hung, J.A. Bennett, F.A. Garcia-Pastor, M. Di Michlel, J.-Y. Buffiere, T.J.A. Doel, P. Bowen, P.J. Withers, Fatigue crack growth and load redistribution in Ti/SiC composites observed in situ, Acta Materialia 57 (2) (2009) 590–599.
[11] E. Ferrié, J.-Y. Buffière, W. Ludwig, A. Gravouil, L. Edwards, Fatigue crack propagation: In situ visualization using X-ray microtomography and 3D simulation using the extended finite element method, Acta Materialia 54 (4) (2006) 1111–1122.
[12] M.R. Parry, S. Syngellakis, I. Sinclair, Numerical modelling of combined roughness and plasticity induced crack closure effects in fatigue, Materials Science and Engineering A 291 (1–2) (2000) 224–234.
[13] N. Kamp, M.R. Parry, K.D. Singh, I. Sinclair, Analytical and finite element modelling of roughness induced crack closure, Acta Materialia 52 (2) (2004) 343–353.
[14] K.H. Khor, J.-Y. Buffière, W. Ludwig, I. Sinclair, High resolution X-ray tomography of micromechanisms of fatigue crack closure, Scripta Materialia 55 (1) (2006) 47–50.
[15] K.D. Singh, K.H. Khor, I. Sinclair, Roughness- and plasticity-induced fatigue crack closure under single overloads: Analytical modelling, Acta Materialia 54 (17) (2006) 4405–4414.
[16] N. Kamp, N. Gao, M.J. Starink, I. Sinclair, Influence of grain structure and slip planarity on fatigue crack growth in low alloying artificially aged 2xxx aluminium alloys, International Journal of Fatigue 29 (5) (2007) 869–878.
[17] K.D. Singh, K.H. Khor, I. Sinclair, Finite element and analytical modelling of crack closure due to repeated overloads, Acta Materialia 56 (4) (2008) 835–851.
[18] W. Ludwig, J.Y. Buffiere, S. Savelli, P. Cloetens, Study of the interaction of a short fatigue crack with grain boundaries in a cast Al alloy using X-ray microtomography, Acta Materialia 51 (3) (2003) 585–598.
[19] L. Salvo, M. Suéry, A. Marmottant, N. Limodin, D. Bernard, 3d imaging in material science: Application of X-ray tomography, Comptes Rendus Physique 11 (9–10) (2010) 641–649.
[20] J.-Y. Buffiere, E. Ferrié, H. Proudhon, W. Ludwig, Three-dimensional visualisation of fatigue cracks in metals using high resolution synchrotron X-ray micro-tomography, Materials Science and Technology 22 (9) (2006) 1019–1024.
[21] J.-C. Labiche, O. Mathon, S. Pascarelli, M.A. Newton, G. Ferre, C. Curfs, G. Vaughan, A. Homs, D. Fernandez Carreiras, Invited article: The fast readout low noise camera as a versatile X-ray detector for time resolved dispersive extended X-ray absorption fine structure and diffraction studies of dynamic problems in materials science, chemistry, and catalysis, Review of Scientific Instruments 78 (9) (2007) 091301.
[22] J.C. Russ, The Image Processing Handbook, 2nd edn., CRC Press, 1994.
[23] P. Cloetens, M. Pateyron-Salome, J.-Y. Buffiere, G. Peix, J. Baruchel, F. Peyrin, M. Schlenker, Observation of microstructure and damage in materials by phase sensitive radiography and tomography, Journal of Applied Physics 81 (9) (1997) 5878–5886.
[24] K. Solanki, S.R. Daniewicz, J.C. Newman, Finite element analysis of plasticity-induced fatigue crack closure: An overview, Engineering Fracture Mechanics 71 (2) (2004) 149–171.
[25] Standard Test Method for Measurement of Fatigue Crack Growth Rates, Annual Book of ASTM Standards, vol. E647-95, ASTM, Philadelphia, 1995.
[26] K. Minakawa, A.J. Mc Evily, On crack closure in the near-threshold region, Scripta Metallurgica 15 (6) (1981) 633–636.
[27] N. Walker, C.J. Beevers, Fatigue crack closure mechanism in titanium, Fatigue of Engineering Materials and Structures 1 (1) (1979) 135–148.
[28] S. Suresh, G.F. Zamiski, R.O. Ritchie, Oxide-induced crack closure: an explanation for near-threshold corrosion fatigue crack growth behavior, Metallurgical Transactions. A, Physical Metallurgy and Materials Science 12 (8) (1981) 1435–1443.
[29] W.O. Soboyejo, J.F. Knott, Investigation of crack closure and the propagation of semi-elliptical fatigue cracks in Q1N (HY80) pressure vessel steel, International Journal of Fatigue 17 (8) (1995) 577–581.
[30] R. Branco, D.M. Rodrigues, F.V. Antunes, Influence of through-thickness crack shape on plasticity induced crack closure, Fatigue and Fracture of Engineering Materials and Structures 31 (2) (2008) 209–220.
[31] F.V. Antunes, J.M. Ferreira, C.M. Branco, J. Byrne, Stress intensity factors for tunnelling corner cracks under mode i loading, Fatigue and Fracture of Engineering Materials and Structures 23 (1) (2000) 81–90.
[32] S. Suresh, Fatigue of Materials, 1st edition, Cambridge University Press, Cambridge, 1994.
[33] B. Budiansky, J.W. Hutchinson, Analysis of closure in fatigue crack growth, Journal of Applied Mechanics Transactions ASME 45 (2) (1978) 267–276.
[34] R.O. Ritchie, Mechanisms of fatigue crack propagation in metals, ceramics and composites: Role of crack tip shielding, Materials Science and Engineering 103 (1) (1988) 15–28.
[35] K.T. Rao Venkateswara, R.O. Ritchie, Fatigue crack propagation and cryogenic fracture toughness behavior in powder metallurgy aluminum–lithium alloys, Metallurgical Transactions. A, Physical Metallurgy and Materials Science 22A (1) (1991) 191–202.

[36] E. Ferrié, J.-Y. Buffiere, W. Ludwig, 3D characterisation of the nucleation of a short fatigue crack at a pore in a cast al alloy using high resolution synchrotron microtomography, International Journal of Fatigue 27 (10) (2005) 1215–1220.
[37] W. Ludwig, P. Reischig, A. King, M. Herbig, E.M. Lauridsen, G. Johnson, T.J. Marrow, J.Y. Buffiere, Three-dimensional grain mapping by X-ray diffraction contrast tomography and the use of Friedel pairs in diffraction data analysis, Review of Scientific Instruments 80 (3) (2009) 033905.
[38] M. Herbig, A. King, P. Reischig, H. Proudhon, E.M. Lauridsen, J. Marrow, J.-Y. Buffiere, W. Ludwig, 3-D growth of a short fatigue crack within a polycrystalline microstructure studied using combined diffraction and phase-contrast X-ray tomography, Acta Materialia 59 (2) (2011) 590–601.
[39] H. Proudhon, S. Forest, W. Ludwig, Large scale finite element simulations of polycrystalline aggregates: applications to X-ray diffraction and imaging for fatigue metal behaviour, in: N. Hansen, D. Juul Jensen, S.F. Nielsen, H.F. Poulsen, B. Ralph (Eds.), Challenges in Materials Science and Possibilities in 3D and 4D Characterization Techniques, 31st Risö International Symposium on Materials Science, Roskilde, Denmark, 2010, pp. 121–139.